

Plasmonic light harvesting for multicolor infrared thermal detection

Feilong Mao,¹ Jinjin Xie,¹ Shiyi Xiao,¹ Susumu Komiya,² Wei Lu,³ and Lei Zhou,^{1,4}
and Zhenghua An,^{1,*}

¹ Institute of Advanced Materials, State Key Laboratory of Surface Physics and Key Laboratory of Micro and Nano Photonic Structures (Ministry of Education), Fudan University, Shanghai 200433, China

² Department of Basic Science, University of Tokyo, Komaba 3-8-9, Meguro-ku, Tokyo 153-8902, Japan
³ National Laboratory for Infrared Physics, Shanghai Institute of Technical Physics, Chinese Academy of Sciences,

Shanghai 200083, China

⁴ phzhou@fudan.edu.cn

*anzhenghua@fudan.edu.cn

Abstract: Here we combined experiments and theory to study the optical properties of a plasmonic cavity consisting of a perforated metal film and a flat metal sheet separated by a semiconductor spacer. Three different types of optical modes are clearly identified—the propagating and localized surface plasmons on the perforated metal film and the Fabry-Perot modes inside the cavity. Interactions among them lead to a series of hybridized eigenmodes exhibiting excellent spectral tunability and spatially distinct field distributions, making the system particularly suitable for multicolor infrared light detections. As an example, we design a two-color detector protocol with calculated photon absorption efficiencies enhanced by more than 20 times at both colors, reaching ~42.8% at $f_1 = 20.0\text{THz}$ ($15\mu\text{m}$ in wavelength) and ~46.2% at $f_2 = 29.5\text{THz}$ (~ $10.2\mu\text{m}$) for a $1\mu\text{m}$ total thickness of sandwiched quantum wells.

©2013 Optical Society of America

OCIS codes: (250.5403) Plasmonics; (040.5160) Photodetectors; (040.3060) Infrared.

References and links

1. A. Krier, *Mid-Infrared Semiconductor Optoelectronics* (Springer, 2005).
2. H. Schneider and H. C. Liu, *Quantum Well Infrared Photodetectors* (Springer, 2007).
3. A. Rogalski, “Material considerations for third generation infrared photon detectors,” *Infrared Phys. Technol.* **50**(2-3), 240–252 (2007).
4. D. I. Ellis and R. Goodacre, “Metabolic fingerprinting in disease diagnosis: biomedical applications of infrared and Raman spectroscopy,” *Analyst (Lond.)* **131**(8), 875–885 (2006).
5. A. Rogalski, J. Antoszewski, and L. Faraone, “Third-generation infrared photodetector arrays,” *J. Appl. Phys.* **105**(9), 091101 (2009).
6. J. Faist, F. Capasso, D. L. Sivco, C. Sirtori, A. L. Hutchinson, and A. Y. Cho, “Quantum Cascade Laser,” *Science* **264**(5158), 553–556 (1994).
7. S. D. Gunapala, S. V. Bandara, J. K. Liu, C. J. Hill, S. B. Rafol, J. M. Mumolo, J. T. Trinh, M. Z. Tidrow, and P. D. LeVan, “ 1024×1024 pixel mid-wavelength and long-wavelength infrared QWIP focal plane arrays for imaging applications,” *Semicond. Sci. Technol.* **20**(5), 473–480 (2005).
8. E. L. Dereniak and G. D. Boreman, *Infrared Detectors and Systems* (Wiley, New York, 1996), Chap. 8.
9. S. D. Gunapala, S. V. Bandara, J. K. Liu, J. M. Mumolo, D. Z. Ting, C. J. Hill, J. Nguyen, B. Simolon, J. Woolaway, S. C. Wang, W. Li, P. D. LeVan, and M. Z. Tidrow, “Demonstration of Megapixel Dual-Band QWIP Focal Plane Array,” *J. Quantum Electron.* **46**(2), 285–293 (2010).
10. S. S. Li, “Recent progress in quantum well infrared photodetectors and focal plane arrays for IR imaging applications,” *Mater. Chem. Phys.* **50**(3), 188–194 (1997).
11. S. D. Gunapala, S. V. Bandara, J. K. Liu, S. B. Rafol, J. M. Mumolo, C. A. Shott, R. Jones, J. Woolaway II, J. M. Fastenau, A. K. Liu, M. Jhabvala, and K. K. Choi, “ 640×512 pixel narrow-band, four-band, and broad-band quantum well infrared photodetector focal plane arrays,” *Infrared Phys. Technol.* **44**(5-6), 411–425 (2003).
12. K. K. Choi, M. D. Jhabvala, and R. J. Peralta, “Voltage-Tunable Two-Color Corrugated-QWIP Focal Plane Arrays,” *IEEE Electron. Dev. Lett.* **29**(9), 1011–1013 (2008).
13. S. C. Lee, S. Krishna, and S. R. J. Brueck, “Quantum dot infrared photodetector enhanced by surface plasma wave excitation,” *Opt. Express* **17**(25), 23160–23168 (2009).

14. C. C. Chang, Y. D. Sharma, Y. S. Kim, J. A. Bur, R. V. Shenoi, S. Krishna, D. H. Huang, and S. Y. Lin, "A Surface Plasmon Enhanced Infrared Photodetector Based on InAs Quantum Dots," *Nano Lett.* **10**(5), 1704–1709 (2010).
15. V. E. Ferry, L. A. Sweatlock, D. Pacifici, and H. A. Atwater, "Plasmonic Nanostructure Design for Efficient Light Coupling into Solar Cells," *Nano Lett.* **8**(12), 4391–4397 (2008).
16. G. W. Lu, B. L. Cheng, H. Shen, Y. L. Zhou, Z. H. Chen, G. Z. Yang, G. Tillement, S. Roux, and P. Perriat, "Fabry-Perot type sensor with surface plasmon resonance," *Appl. Phys. Lett.* **89**, 22394 (2006).
17. B. S. Dennis, V. Aksyuk, M. I. Haftel, S. T. Koev, and G. Blumberg, "Enhanced coupling between light and surface plasmons by nano-structured Fabry-Perot resonator," *J. Appl. Phys.* **110**(6), 066102 (2011).
18. W. Wu, A. Bonakdar, and H. Mohseni, "Plasmonic enhanced quantum well infrared photodetector with high detectivity," *Appl. Phys. Lett.* **96**(16), 161107 (2010).
19. CONCERTO 7.0, Vector Fields Limited, England (2008).
20. Y. Todorov, A. M. Andrews, I. Sagnes, R. Colombelli, P. Klang, G. Strasser, and C. Sirtori, "Strong Light-Matter Coupling in Subwavelength Metal-Dielectric Microcavities at Terahertz Frequencies," *Phys. Rev. Lett.* **102**(18), 186402 (2009).
21. More accurately, in the deep subwavelength region(i.e., $S < \lambda_s/2n_{\text{GaAs}}$), f_1 is insensitive to S , as will be seen in Fig. 3.
22. T. W. Ebbesen, H. J. Lezec, H. F. Ghaemi, T. Thio, and P. A. Wolff, "Extraordinary optical transmission through sub-wavelength hole arrays," *Nature* **391**(6668), 667–669 (1998).
23. Y. W. Jiang, L. D. C. Tzeng, Y. H. Ye, Y. T. Wu, M. W. Tsai, C. Y. Chen, and S. C. Lee, "Effect of Wood's anomalies on the profile of extraordinary transmission spectra through metal periodic arrays of rectangular subwavelength holes with different aspect ratio," *Opt. Express* **17**(4), 2631–2637 (2009).
24. C. Y. Chen, M. W. Tsai, T. H. Chuang, Y. T. Chang, and S. C. Lee, "Extraordinary transmission through a silver film perforated with cross shaped hole arrays in a square lattice," *Appl. Phys. Lett.* **91**(6), 063108 (2007).
25. H. Wang, Z. An, C. Qu, S. Xiao, L. Zhou, S. Komiyama, W. Lu, X. Shen, and P. Chu, "Optimization of Optoelectronic Plasmonic Structures," *Plasmonics* **6**(2), 319–325 (2011).
26. A. Mary, S. G. Rodrigo, L. Martin-Moreno, and F. J. García-Vidal, "Theory of light transmission through an array of rectangular holes," *Phys. Rev. B* **76**(19), 195414 (2007).
27. The formula for n_{eff} in Eq. (2) applies to the case where the insulators on two sides of the metal layer are half-infinite. Here we use same formula to roughly estimate n_{eff} value for our plasmonic cavity case.
28. Due to the limitation of $L < P$ for a cross hole array, there remains a small fraction of PSP $\{0, \pm 1\}$ contribution for f_1 in H-cavity.
29. The PSP $\{0, \pm 2\}$ is readily coupled to LSP which is predicted from Eq. (2) to be near 40THz. As a result, PSP $\{0, \pm 2\}$ is highly hybridized with LSP mode.
30. y-polarized excitation is used in FDTD simulation, therefore $E_x \approx 0$ for all resonant modes, and only $\{0, \pm 1\}$ (but not $\{\pm 1, 0\}$) PSP mode contributes in calculations. In experiments, both $\{\pm 1, 0\}$ and $\{0, \pm 1\}$ modes contribute equally to the measured reflection spectra since cross hole shape is insensitive to polarization.
31. J. L. Pan and C. G. Fonstad, Jr., "Theory, fabrication and characterization of quantum well infrared photodetectors," *Mater. Sci. Eng. Rep.* **28**(3-4), 65–147 (2000).
32. W. Wu, A. Bonakdar, and H. Mohseni, "Plasmonic enhanced quantum well infrared photodetector with high detectivity," *Appl. Phys. Lett.* **96**(16), 161107 (2010).
33. D. Dini, R. Köhler, A. Tredicucci, G. Biasiol, and L. Sorba, "Microcavity Polariton Splitting of Intersubband Transitions," *Phys. Rev. Lett.* **90**(11), 116401 (2003).
34. In case of 45° edge facet incidence, the device responses only half of the unpolarized excitation due to the selection rule. For optimized polarization of the excitation, the simulated efficiencies reach ~4% for our QWs, which agree well with the previously reported values in Ref.[2].
35. These enhancement factors increase at lower electron densities. For example, at $N_s = 1 \times 10^{11}/\text{cm}^2$, the enhancement factors are ~55 at f_1 (cavity: 23.0%; non-plasmonic: 0.84%; single-layer: 2.7%) and ~45 at f_2 (cavity: 18.8%; non-plasmonic: 0.84%; single-layer: 0.3%).
36. X. L. Liu, T. Tyler, T. Starr, A. F. Starr, N. M. Jokerst, and W. J. Padilla, "Taming the Blackbody with Infrared Metamaterials as Selective Thermal Emitters," *Phys. Rev. Lett.* **107**(4), 045901 (2011).

1. Introduction

Infrared (IR) technology is developing rapidly in recent decades due to numerous application requests from sciences, health, security and industry [1–6]. Semiconductor-based quantum well infrared photodetectors (QWIPs) [1,2] are widely used in this area, owing mainly to their excellent performance, high yield in semiconductor production, and feasible operability in highly uniform large focal plane arrays. To date, megapixel size QWIPs have already been realized [7]. However, most of QWIPs developed so far are single-color devices. The feasibility of single-color application relies on the gray-body assumption of the targets whose emission can be described as $I(\varepsilon_{em}, T) = \varepsilon_{em} \cdot f_{Planck}(T)$, where ε_{em} , and $f_{Planck}(T)$ are the emissivity and Planck's distribution of black-body radiation with T being the temperature of

the target. The spectroscopic features of the target's emission are therefore completely neglected. These characteristics restrict single-color QWIPs from wider applications such as remote sensing where accurate temperature sensing of the target with unknown emissivity is needed or gas monitoring in which the spectroscopic fingerprints are crucial [8]. Also, in the imaging applications, simultaneous detection at several wavelengths is highly desired to obtain the full message of a target (both ϵ_{em} patterns and T distributions) [9]. As a result, multicolor IR detections are attracting more and more attention recently.

Some efforts have already been devoted to designing multicolor QWIPs [9–11], but attentions were mostly paid to optimizing the material growth and device processing. The problem of light-coupling efficiency in such devices was, however, generally overlooked. While a grating coupler can couple light into optoelectronic devices with reasonable efficiency, it typically works for only a single wavelength with relatively narrow bandwidth [2,11,12]. For a recently proposed multicolor detector, photo-coupler consisting of multiple independently optimized gratings was designed [9,11]. However, it appeared rather complicated and its performance seemed to be still restricted by its low light coupling efficiencies. A co-located and versatile photo-coupler functioning for multicolor detection is therefore highly desirable.

Stimulated by the discovery of extraordinary optical transmission in periodically perforated metallic plate a decade ago, plasmonic structures began to draw intensive attention in designing high-efficiency photo-couplers for optoelectronic applications [13–15], thanks to their strong capabilities of coupling far-field light to near field and controlling the light in a nano-scale. Meanwhile, coupling of different optical modes such as plasmonic modes and photonic Fabry-Perot (FP) modes can enhance the photodetection and biosensing sensitivities [16,17]. However, so far, only a few designed or fabricated (two-dimensional) plasmonic photo-couplers are reported for QWIP applications and also are restricted to single-color applications [14,18], since typically these systems only support a single type of plasmonic mode. In this Letter, we show that a three-dimensional plasmonic cavity combining a perforated plasmonic metal with a FP cavity exhibits interesting optical properties. Interactions among resonant modes of different origins form a rich eignemode spectrum with spatially well-separated wavefunctions, making the system particularly suitable for high-sensitive multi-color detections. As an illustration, we design a realistic two-color infrared detector by combining our cavity with two quantum-well (QW) layers, and show that the detection performances of the device can be enhanced significantly with respect to the non-plasmonic case.

2. Results and discussion

Figure 1(a) schematically shows the designed structure, in which the top metal layer is a Au film perforated with an array of cross-shaped holes and the bottom one is a continuous Au film. A dielectric spacer of thickness S is adopted to separate the two gold films. Each cross hole has a length L , width W , and the periodicity of the hole array is P . We first employed both finite-difference time-domain (FDTD) simulation [19] and experiment to characterize the optical properties of such a system. We fabricated a series of cavity samples with lateral size $36 \mu\text{m} \times 36 \mu\text{m}$ in thickness and the dielectric spacer is a GaAs film. Figure 1(b) shows the scanning electron microscope (SEM) top-view image of one of our samples. Due to the continuous Au film on the back, our systems do not allow light transmission, and therefore, we only focus on its reflection properties in what follows. The reflection spectra of experimentally fabricated samples were measured under an infrared microscope (Bruker HYPERION 1000) with collimated light beam by using a Cassegrain lens with effective N.A. of 0.4 ($+/-23.6^\circ$) and shade N.A. of 0.17 ($+/-9.8^\circ$). Figure 1(c) compares the measured reflection spectra for two samples with the same lateral structure but with different thickness

S. In the studied frequency range, three resonance dips are clearly identified for each sample, indicating that photons can be significantly coupled into the devices at these frequencies. These are the precise signatures of the resonance eigenmodes for the designed system. The FDTD calculated reflection spectra are shown in Fig. 1(d), from which three sharp resonances can also be identified for each sample, whose positions are in excellent agreement with experiment. However, the calculated resonance dips are much sharper than the measured ones, probably due the structural imperfections of the fabricated samples. Comparisons between calculations and measurements also identity that the dip at ~ 31.4 THz in the experimental spectra for the $S = 0.8\mu\text{m}$ sample is induced by the incident angle distribution of the collimated infrared light beam used in the spectral measurements. Our additional simulation work (not shown here) indicate that it originates from a horizontal FP-like resonance which is reported in Ref [20].

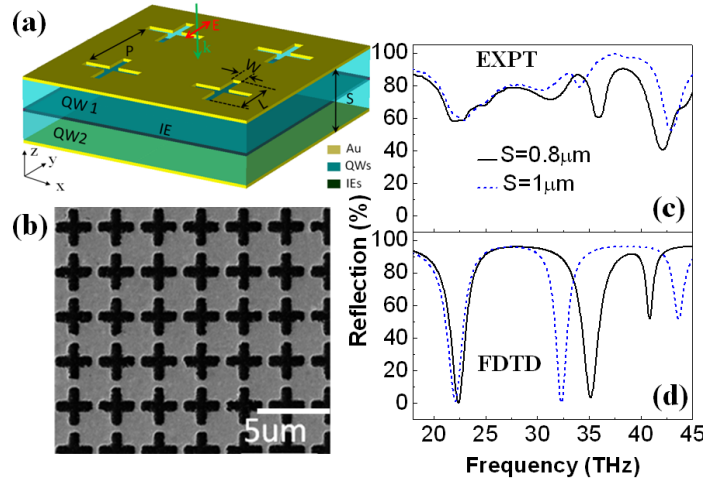


Fig. 1. (Color) Schematic diagram of a plasmonic cavity designed for two-color quantum well infrared photodetectors. (b) A top view SEM image of a typical sample. (c) Experimental and (d) FDTD simulation reflection spectra of plasmonic cavities with $S = 0.8\mu\text{m}$ (solid black) and $1\mu\text{m}$ (dash blue). The lateral geometric parameters are fixed at $P = 3\mu\text{m}$, $L = 2.6\mu\text{m}$, $W = 0.52\mu\text{m}$

To understand the physical origins of those optical modes, we systematically investigated the dependences of resonance frequencies on the geometrical parameters P , L , and S with $W/L = 0.2$ fixed. We first focus on the lowest-order resonance f_1 . Figure 2 depicts how f_1 depends on the array period P and cross-hole length L . Here we fix $S = 1\mu\text{m}$ and our later analysis suggests that f_1 is rather insensitive to S [21]. We note that f_1 is generally a decreasing function of both P and L , and therefore, to obtain a given f_1 , L must increase when P decreases and vice versa. Without losing generality, we explicitly plotted the equal-frequency line for $f_1 = 20$ THz in Fig. 2 as a solid curve. As $L \rightarrow 0$ (i.e., very small hole size), f_1 becomes insensitive to the hole size and depends solely on the array period. In this limiting case, the resonance is dominated by the periodicity-induced surface plasmon (PSP) [22]. Treating Au as a good metal with an infinitely negative ϵ and assuming the thickness of the GaAs spacer is infinite, we can approximate the frequency of such a resonance by,

$$f_{\text{PSP}} \approx \frac{c}{P\sqrt{\epsilon_{\text{GaAs}}}} \sqrt{i^2 + j^2} \quad (1)$$

where $\{i, j\}$ are integers and equal to $\{1, 0\}$ or $\{0, 1\}$ for the lowest order resonance f_1 in Fig. 2, c is the light speed in vacuum and ϵ_{GaAs} is the dielectric constant of the substrate. On the

other hand, as $L \rightarrow P$ (i.e., large hole size), the resonance f_1 is contributed mainly by the fundamental localized surface plasmon (LSP) of the cross holes [23–26], and can be approximately given by

$$f_{\text{LSP}} = \frac{c}{2L \cdot n_{\text{eff}}} \quad (2)$$

with $n_{\text{eff}} \approx \sqrt{(\epsilon_{\text{GaAs}} + \epsilon_{\text{air}})/2}$ being the effective refraction index of the surrounding medium [27]. Figure 2 already suggested that all equal-frequency lines follow the same trend as the 20 THz case. To quantify this universal behavior, we re-plotted *all* calculated results with respect to $Pf_1(\sqrt{\epsilon_{\text{GaAs}}}/c)$ and $Lf_1(\sqrt{\epsilon_{\text{GaAs}}}/c)$ in the inset to Fig. 2. All data points converge to the same curve, revealing the geometrical nature of such resonant modes. Available experimental data (hollow stars) further validate this universal behavior. To ease further discussions, we pick out eight points (A, B, C, D, E, F, G, H) from the solid curve in Fig. 2 ($f_1 = 20\text{THz}$), with the A-structure defining the small hole limit (with PSP-like mode) while the H-cavity defining the large hole limit (with LSP-like mode) [28]. Note that both PSP and LSP modes contribute more or less for all structures studied in this work. The difference between A and H is that A (H) is dominated by PSP (LSP) mode with a very small contribution from LSP (PSP) mode.

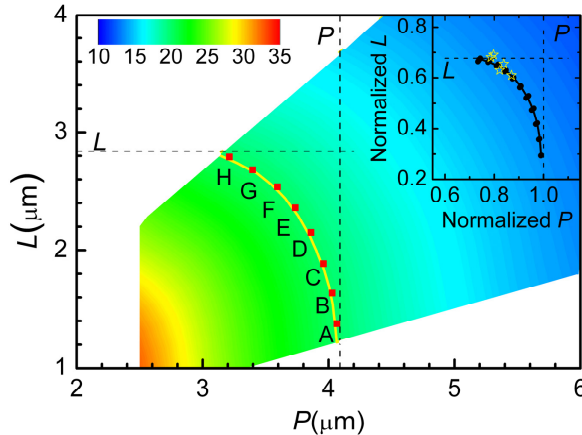


Fig. 2. Color contour plot of the lowest resonance frequency f_1 against P and L for the studied plasmonic cavities according to FDTD simulation, with solid curve depicting the equifrequency contour line with $f_1 = 20\text{THz}$. Inset shows same results with normalized P (i.e., $Pf_1(\epsilon_{\text{GaAs}}^{1/2}/c)$) and normalized L , (i.e., $Lf_1(\epsilon_{\text{GaAs}}^{1/2}/c)$). Hollow stars are derived from experimentally measured spectra.

We next study how the resonance modes depend on the cavity thickness S , paying attention to not only the lowest-order resonance but also higher-order ones. Choosing the lateral geometry as the A structure, we calculated by FDTD the reflection spectra for cavities with different S , and then plotted the reflectance in Fig. 3(a) as a function of $1/S$ and frequency. As denoted by vertical lines in Fig. 3(a), the PSP resonance modes remain almost unchanged as S becomes large, especially for the lowest two modes with indexes {0,1} and {1,1} [29]. Meanwhile, bulk cavity modes appear in the thick-cavity region (sloped lines in the left-down corner), and can be described by,

$$f_{\text{FP}}^{(n)} = n \cdot \frac{c}{2S\sqrt{\epsilon_{\text{GaAs}}}} \quad (3)$$

with n being a positive integer. In the down-right region of Fig. 3(a) where both PSP and FP mechanisms are present, there appear plenty of hybridized resonance modes which can be approximately described by,

$$f(i, j, n) = \frac{c}{2\pi} \cdot \sqrt{\left| \vec{k}_{\text{PSP}} \right|^2 + \left| \vec{k}_{\text{FP}} \right|^2} \approx \frac{c}{\sqrt{\epsilon_{\text{GaAs}}}} \sqrt{\frac{i^2 + j^2}{P^2} + \frac{n^2}{4S^2}} \quad (4)$$

For example, we plot in Fig. 3(a) the calculated dispersion curves for the {0,1,1} and {1,1,1} modes as dot-dash lines, which match excellently with the FDTD calculated reflection dips.

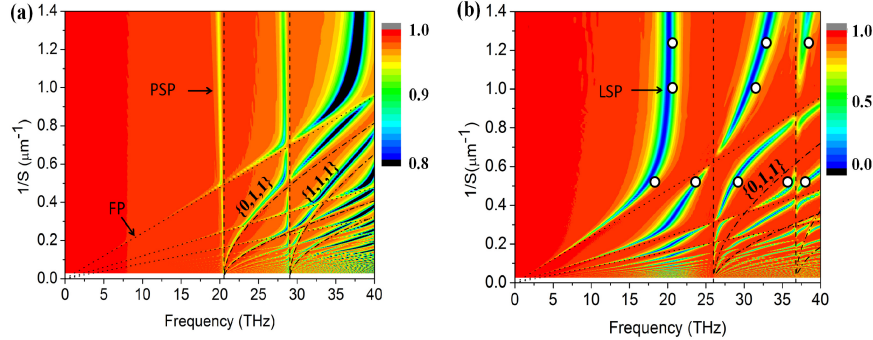


Fig. 3. Color contour plot of the calculated reflection against f and $1/S$ for plasmonic cavities with lateral geometry chosen as (a) A-structure and (b) H-structure, where S is the cavity thickness. In both (a) and (b), the sloped dotted lines describes the Fabry-Perot (FP) cavity modes [Eq. (3)], the vertical dashed lines denote the PSP modes based on Eq. (1), and the parabolic-like curves describes the hybridized modes based on Eq. (4). The hollow circles in (b) display the experimentally measured resonances for $S = 0.8\mu\text{m}, 1\mu\text{m}$ and $2\mu\text{m}$.

We now study the case when the lateral geometry is chosen as the H-structure, in which the LSP dominates the plasmonic surface mode (f_1). As shown in Fig. 3(b) where the reflection spectra are plotted, the resonant modes exhibit dramatically different behaviors as compared with the A-cavity case (Fig. 3(a)). Available experimental data are denoted in Fig. 3(b) as open circles, agreeing well with the FDTD results. For comparison, resonances predicted by Eqs. (1), (3) and (4) are again drawn as dotted lines in Fig. 3(b). Agreement is observed only for pure FP modes in the low-frequency region where plasmonic modes do not appear. In the high frequency region where LSP mode comes in, a series of *hybridized* eigenmodes are formed, with resonance frequencies deviating significantly from the predictions based on Eqs. (3) and (4).

The dramatic difference between the A and H cases already implied the different interaction mechanisms between the LSP (PSP) and the FP modes. To illustrate, we numerically calculated the electric-field distributions for (nearly) pure FP, LSP and PSP modes (FP: $P = 3.2\mu\text{m}$, $L = 2.8\mu\text{m}$, $S = 3.3\mu\text{m}$; LSP: $P = 3.2\mu\text{m}$, $L = 2.8\mu\text{m}$, $S = 1\mu\text{m}$; PSP: $P = 4.1\mu\text{m}$, $L = 1.4\mu\text{m}$, $S = 1\mu\text{m}$. W is fixed to be $0.52\mu\text{m}$). Figure 4 depicts the distributions of E_y and E_z on the x - y plane located at the cavity center for three modes [30]. While a FP mode exhibits predominantly E_y field component on the x - y plane, the PSP mode has very small E_y component but has large E_z component, which is a common feature for a surface plasmon polariton on a flat Au surface. Due to their orthogonal field components, these two modes have very weak coupling strength despite of their large spatial overlapping. However, as shown in Figs. 4(d) and 4(e), the LSP mode has more complicated fringe field distributions around the cross holes, and the maximum values of E_y and E_z components differ only by a factor of about ~ 3 , implying both components are important. Noting that the E_y component of LSP mode matches the dominant component (i.e., E_y) of FP mode, LSP and FP modes not only overlap spatially, but also can interact strongly; Similarly, the E_z component of LSP

mode allows its strong interaction with PSP (whose E_z is dominant). This well explains why the optical modes are hybridized considerably as shown in Fig. 3(b) and those hybridized modes deviate significantly from Eq. (4) obtained under weak-coupling assumption. It is noteworthy to point out that the unique polarization property of LSP mode (with both large E_y and E_z components) not only allows it to efficiently couple with PSP mode (Fig. 2) and FP mode (Fig. 3(b)), but also enables its coupling with external plane waves, which is critical for photodetection applications..

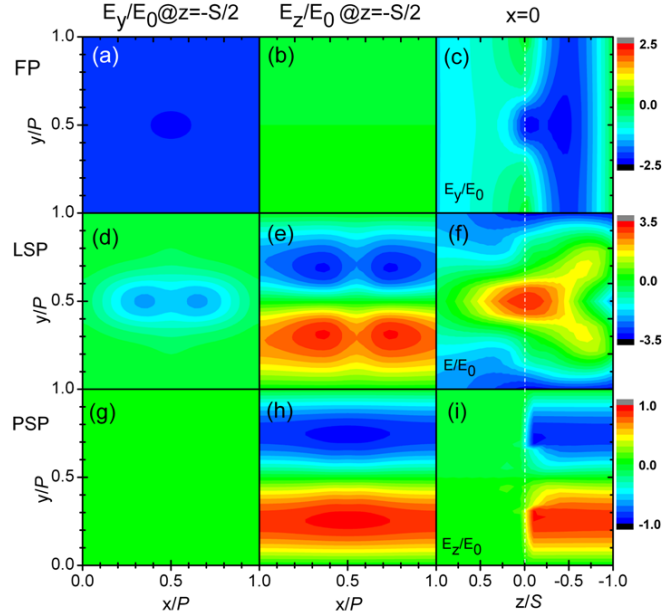


Fig. 4. Color contour plot of the simulated electric-field distribution of the photonic FP mode (a)-(c), plasmonic LSP (d)-(f), and PSP (g)-(i). (a),(d),(g) and (b),(e),(f) are the E_y and E_z distribution over x - y plane (at the cavity center, i.e., $z = -S/2$) for FP, LSP and PSPs. (c),(f),(i) are the E_y, E_z distributions over y - z plane (at $x = 0$) of FP, LSP and PSP modes, respectively. $z/S = 0$ and $z/S = -1$ refer to the positions of top and bottom Au/GaAs interfaces. (j) Ratio between the averaged amplitudes of E_y and E_z components on xy -plane, i.e., $\langle E_y \rangle / \langle E_z \rangle$ values for FP, LSP and PSP states as functions of depth z

The rich optical properties of these plasmonic cavities, contributed by the fascinating interactions of optical modes with different origins, offer the systems many opportunities for designing optoelectronic devices facing different applications. For example, noting that the PSP-like hybridized modes generally have large quality (Q) factors (see Fig. 3(a)) while the LSP-like ones generally exhibit wider and deeper reflection dips (see Fig. 3(b)), one may “tune” the optical resonance to be more PSP-like or FP-like in applications where a higher Q -factor is desired, but be more LSP-like when the coupling efficiency with external light is more important. In what follows, we design a realistic two-color detector by combining our plasmonic cavity with QW active medium, and test the performance of such a device.

Since the coupling with external light is crucial for detector performance, we choose the H-structure to design a two-color detector. We utilize LSP-like state for lower detection frequency (f_1) and strongly hybridized state for the higher one (f_2). We set $S = 1\mu\text{m}$ without losing generality, although we have much wider freedoms to achieve our design with target functionalities. As schematically shown in Fig. 1(a), we assume that two photo-active QW layers (denoted by QW1 and QW2) will be inserted into our plasmonic cavity, aiming to response at two different working frequencies ($f_1 = 20.0\text{THz}$ and $f_2 = 29.5\text{THz}$) matching the resonances of the plasmonic cavity. To determine the optimized positions of these two QW

layers, we calculated the *average* field enhancements on different *xy*-planes within the cavity by

$$\frac{\langle E_z^2 \rangle}{\langle E_0^2 \rangle} = \int \frac{|E_z|^2 dx dy}{|E_0|^2 P^2} \quad (5)$$

where E_0 and E_z represent the incident and local electric fields and $\langle \dots \rangle$ stands for field amplitude average on the *x*-*y* plane. Only E_z -component is considered because the quantum well is only sensitive to this field component [31]. Therefore, the profiles of $\langle E_z^2 \rangle / \langle E_0^2 \rangle$ represent the abilities of two QW layers to absorb light waves. Figure 5 shows that the local field is strongly enhanced for two target frequencies f_1 and f_2 . While the peak enhancement factors $\langle E_z^2 \rangle / \langle E_0^2 \rangle$ had already reached 7 and 4.5 for two frequencies, we note that they are actually much higher if we compare with the case without any plasmonic coupler. When infrared lights impinge on the GaAs medium normally, the electric field is reduced by a factor of $\langle E^2 \rangle_{\text{no-plasmonic}} / \langle E_0^2 \rangle \approx 0.21$. Therefore, the real enhancements achieved with our plasmonic cavity are $\langle E_z^2 \rangle_{\text{plasmonic}} / \langle E^2 \rangle_{\text{no-plasmonic}} \approx 33.3$ and 21.4 for two colors, respectively. For comparison, a previous work of a single-color application only showed $\langle E_z^2 \rangle_{\text{plasmonic}} / \langle E^2 \rangle_{\text{no-plasmonic}} \approx 5$ in a single-layer circular hole array plasmonic coupler [32].

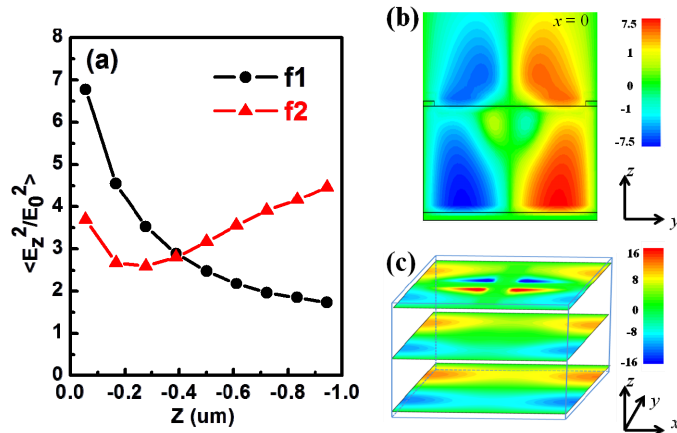


Fig. 5. (a) FDTD calculated profiles of $\langle E_z^2 \rangle / \langle E_0^2 \rangle$ averaged over *x*-*y* plane for the H-cavity with $S = 1\mu\text{m}$ at two resonances $f_1 = 20.0\text{THz}$ and $f_2 = 29.5\text{THz}$. $z = 0$ refers to the top Au/GaAs interface and $z = -1\mu\text{m}$, the bottom one. (b) and (c) FDTD calculated field mapping of E_z component of the highly hybridized mode (at f_2) over *y*-*z*-plane at $x = 0$ (b) and over *xy*-planes at depths of $z = -0.1\mu\text{m}, -0.5\mu\text{m}$ and $-0.9\mu\text{m}$ (c).

We note that two curves in Fig. 5 exhibit distinct z -dependences, which are very helpful for us to select the optimized positions to place the two QW layers. The f_1 -curve is a decreasing function of z , which is again dictated by the “surface” nature of this mode (a nearly pure LSP mode). In contrast, the f_2 -curve exhibits more complicated dependence on z , which is contributed by the “hybridized” nature of this mode. To illustrate, we showed in Fig. 5(b) and 5(c) the distributions of E_z on *yz*-plane (at $x = 0$) and 3 typical *xy*-planes, respectively. The considerable field outside the cavity (Fig. 5(b)) is a clear characteristic of the LSP state. In addition, the LSP field penetrates into the cavity interacting with the plasmonic PSP and photonic FP modes. The induced PSP components are more clearly identified in Fig. 5(c) as the stripe-like distributions over *xy*-plane at several depths, and the

photonic FP fraction is evidenced by the E_y distribution which is though not shown but appears similar to Fig. 4(c). To summarize, the LSP portion not only couples far field excitation into the plasmonic cavity, but also couples to and mediates the mutual couplings between PSP and FP modes, eventually forming highly hybridized resonant state at f_2 . The interactions among different modes result in a complex field pattern, which leads to the nonmonotonous distribution of $\langle E_z^2 \rangle / \langle E_0^2 \rangle$ as shown in Fig. 5(a). The E_z field minimum appearing near $z = -0.2\mu\text{m}$ is induced by the interaction between the LSP and FP modes, where the former provides a non-zero E_z component while the latter causes the field oscillations. As a result, the maximum in the f_2 -curve appears at a position *different* from that of the f_1 -curve, which is the desired property that can be utilized in multi-color optoelectronic applications. We emphasize that it is the interaction between different modes in such a plasmonic cavity that leads to such fascinating behaviors, which are difficult to obtain with a conventional device.

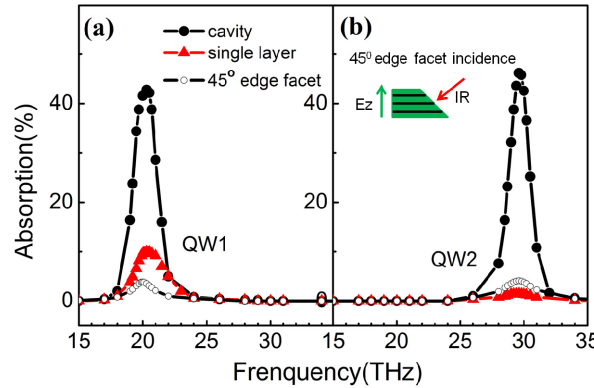


Fig. 6. FDTD calculated absorption spectra of each QW layer, QW1 (a) and QW2 (b), for the designed two-color plasmonic detector (solid dots), a single layer coupler with same cross hole arrays (solid triangles) and 45° edge facet incidence without any metal structures (hollow dots). The cavity is H-structure with $S = 1\mu\text{m}$.

We performed FDTD simulations to quantify the detecting efficiency of the proposed device. In our simulations, we assumed that the permittivity of QWs are given by [33]

$$\epsilon_{i,z}(\omega) = \epsilon_{\text{GaAs}} + \frac{N_s e^2 f_{i,\text{osc}}}{m_0 \epsilon_0 L_{\text{eff}}} \frac{1}{(\omega_i^2 - \omega^2) - i\gamma_i \omega} \quad (6)$$

in which $i = 1,2$ denote the QW number, N_s and $f_{i,\text{osc}} = (2m/\hbar)\omega_i d^2$ are the electron density and inter-subband transition oscillation strength of the i th QW, L_{eff} is the effective QW width, m_0 is electronic rest mass, ω_i are the center angular frequencies of inter-subband transitions, γ_i intersubband linewidth, d the dipole matrix element between the envelope function of two subbands which is set as 2nm here. Note that we have set $\epsilon_x = \epsilon_y = \epsilon_{\text{GaAs}}$ since the QWs are only sensitive the E_z component due to the polarization selection rule. Setting $N_s = 5 \times 10^{11}/\text{cm}^2$, $L_{\text{eff}} = 60\text{nm}$, $\gamma_i = 0.15\omega_i$ based on typical experimental conditions, we performed FDTD simulations to separately calculate the light absorptions in *each* QW layer under normally incident light illuminations. As a reference, we calculated the absorption spectrum of the same QW layer which is standing alone without any plasmonic coupler. In such a case, we studied the 45° edge facet incidence which is commonly used to quick test the QW response to IR light, the incidence schematic diagram is shown in Fig. 6(b) insert, light normally incident to a 45° facet of the QW, and the QW growth direction is the same as E_z .

As an additional reference, we also calculated the absorption spectra for the same QW layer when it is coupled with a conventional single-layer photo-coupler consisting of a metal film perforated with cross-hole array (identical to the top layer in our device). As shown in Fig. 6, the absorption efficiencies of the QWs in our plasmonic cavity reach \sim 42.8% (at $f_1 = 20.0\text{THz}$) and \sim 46.2% (at $f_2 = 29.5\text{THz}$), respectively. In contrast, they are \sim 2.0% at both f_1 and f_2 in the non-plasmonic case [34], and \sim 10.0% at f_1 and \sim 1.46% at f_2 in the single-layer coupler case. The enhancement factors compared to non-plasmonic coupler case are therefore 21.4 at f_1 and 23.1 at f_2 , manifesting the excellent functionality of the designed device [35]. Finally, we mention that a similar work [36] also indicates that metal-dielectric-metal plasmonic structures are very useful in tailoring the single-band or multi-band infrared optical properties and are therefore attractive for thermal infrared applications.

3. Conclusion

We investigated the rich optical properties of a particular plasmonic cavity and designed a realistic multi-color photodetector device. We find that the plasmonic and photonic modes as well as their hybridization in this system can be well adjusted by the geometric parameters including the hole size, array periodicity and semiconductor layer thickness. The spectrally tunable multiple resonances and their spatially distinct profiles well match the multicolor QWIP applications. The absorption efficiencies of an exemplified two-color QWIP are significantly enhanced and reach \sim 42.8% and \sim 46.2% at two colors (20.0THz and 29.5THz), which are more than 20 times higher than the non-plasmonic case.

Acknowledgment

Z. A. thanks Professor Gengfeng Zheng for valuable discussions and suggestions and Professors Xuechu Shen and Zhanghai Chen for assistance during the project. This work was jointly supported by the National Basic Research Program of China Grant No.2009CB929300, the NSFC Contracts No. 10804019/60990321/11174055, Shanghai Science and Technology Committee Contract No. 09dj1400103. Z.A. and S.K. thank Japan Science and Technology Corporation for the financial support.